

Partial-differential-equation-constrained amplitude-based shape detection in inverse acoustic scattering

Seong-Won Na · Loukas F. Kallivokas

Received: 11 May 2006 / Accepted: 10 June 2007 / Published online: 5 September 2007
© Springer-Verlag 2007

Abstract In this article we discuss a formal framework for casting the inverse problem of detecting the location and shape of an insonified scatterer embedded within a two-dimensional homogeneous acoustic host, in terms of a partial-differential-equation-constrained optimization approach. We seek to satisfy the ensuing Karush–Kuhn–Tucker first-order optimality conditions using boundary integral equations. The treatment of evolving boundary shapes, which arise naturally during the search for the true shape, resides on the use of total derivatives, borrowing from recent work by Bonnet and Guzina [1–4] in elastodynamics. We consider incomplete information collected at stations sparsely spaced at the assumed obstacle’s backscattered region. To improve on the ability of the optimizer to arrive at the global optimum we: (a) favor an amplitude-based misfit functional; and (b) iterate over both the frequency- and wave-direction spaces through a sequence of problems. We report numerical results for sound-hard objects with shapes ranging from circles, to penny- and kite-shaped, including obstacles with arbitrarily shaped non-convex boundaries.

Keywords Inverse acoustic scattering · Boundary integral equations · Shape detection · Total differentiation · KKT conditions

1 Introduction

Inverse scattering problems are of considerable practical interest in various areas of science and engineering due, in part, to the ever broadening spectrum of important applications that range from medical, to geophysical, to target identification investigations. In particular, inverse problems arising in acoustics are of relevance in, amongst others, ultrasound imaging (for medical or other non-destructive assessments), seismic imaging, underwater surveillance and target acquisition, and in the detection of objects in the ocean, whether fully submerged or partially buried in the seafloor.

Invariably, in all of the aforementioned areas the common goal is to arrive at a description of unknown parameters of an interrogated object, whether these parameters refer to material properties, boundary conditions, or geometric measures, by, typically, relying on knowledge of input parameters (e.g. interrogating frequencies) and output measurements (e.g. response at coarsely distributed sensor locations). Due to the incomplete data set such problems are inherently ill-posed (and numerically ill-conditioned), with the ill-posedness originating from any or all of three possible sources, namely, solution non-existence, non-uniqueness, and/or (numerical) instability [5–7]. To alleviate or overcome the considerable algorithmic challenges imposed by the ill-posedness, specialized schemes need to be devised. In this article, we provide a description of such a specialized scheme applied to the acoustic case, with, however, sufficient generality to allow the treatment of similar problems in other areas including electromagnetics, elastodynamics, or multi-physics problems.

Partial support for this work was provided by the US National Science Foundation under grant award CMS-0348484.

S.-W. Na · L. F. Kallivokas (✉)
Department of Civil, Architectural and Environmental Engineering,
The University of Texas at Austin, 1 University Station,
C1748, Austin, TX 78712, USA
e-mail: loukas@mail.utexas.edu

2 Background

Of interest here is the problem of recovering the shape of an insonified scatterer from scant measurements of its response when excited by impinging plane waves. We treat the case of a sound-hard scatterer embedded in full-space (Fig. 1). The problem has received considerable attention in the literature; among the many reviews on the topic we mention the works in [8–10]. One may roughly classify the approaches that have been followed, into methods that rely on optimization-based schemes (e.g. [1–4, 11–18]), and methods that do not explicitly seek to minimize a misfit functional (e.g. [19–23]). The advantage of the latter category methods is that the shape reconstruction can be carried out without necessarily relying on a priori information, whereas, when optimization methods are used, the solution feasibility space may be considerably narrowed due to a priori knowledge—almost a necessity for robust solution schemes. In this work we favor optimization methods for the generality they offer and explore continuation algorithms that have, thus far, provided promising results. We remark that a considerable body of work exists where solutions are sought based on complete information: in the context of the shape detection problem of interest in this article, complete information refers to, for example, scattered pressure data that circumscribe the scatterer. Even if such measurements were collected on only a coarse discretization of a boundary surface surrounding the scatterer, they still circumscribe the sought obstacle and are tantamount to a finite-dimensional description of complete information. However, in many engineering applications, obtaining complete information is practically impossible, and thus the focus on the numerical examples in this article is exclusively on problems where the measurement stations are distributed in the backscattered region only.

This study comes closest to the elegant treatment of similar inverse shape detection problems reported by Bonnet, Guzina, and their collaborators in [1–4]. Here we try to improve on the sensitivity to the initial guess they reported, by using amplitude-based misfit functionals, and continuation schemes. In addition, the problem is cast within a systematic partial-differential-equation (PDE)-constrained optimization framework that leads to a set of Karush–Kuhn–Tucker (KKT) conditions, which we then seek to satisfy in an attempt to reconstruct the sought shape.

3 Mathematical modeling

3.1 The forward problem

We are concerned with the classical time-harmonic boundary-value problem that is governed by the Helmholtz equation in two dimensions. Let Γ be a (smooth) closed

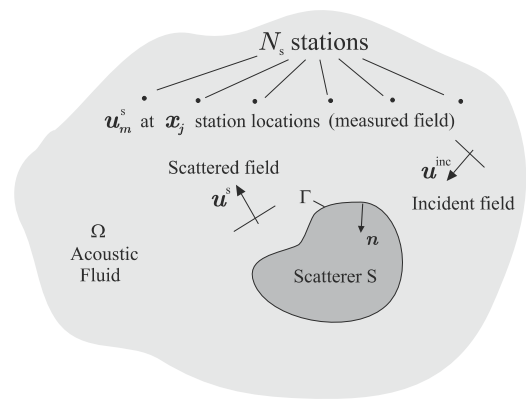


Fig. 1 Scattering from a sound-hard object in full space and sampling stations

surface with exterior $\Omega \subset \mathbb{R}^2$ as shown in Fig. 1. The exterior domain Ω is occupied by a linear, inviscid, and compressible (acoustic) fluid, characterized by wave velocity c . Γ is the bounding surface of an immovable rigid (sound-hard) obstacle S . When S is insonified by an incident plane wave field u^{inc} , the scattered field can be recovered as the solution to the following problem:

$$\Delta u^s(\mathbf{x}) + k^2 u^s(\mathbf{x}) = 0, \quad \mathbf{x} \in \Omega, \tag{1}$$

$$\frac{\partial u^s(\mathbf{x})}{\partial n} = -\frac{\partial u^{inc}(\mathbf{x})}{\partial n}, \quad \mathbf{x} \in \Gamma, \tag{2}$$

$$\lim_{r \rightarrow \infty} \sqrt{r} \left(\frac{\partial u^s}{\partial r} - i k u^s \right) = 0. \tag{3}$$

In these equations u^s denotes scattered pressure; \mathbf{x} is the position vector; \mathbf{n} is the outward unit normal on Γ (pointing to the interior of S); Δ is the Laplace operator; k is the wavenumber ($k = \frac{\omega}{c}$, with ω denoting circular frequency). Condition (3), in which r is radial distance, is the Sommerfeld radiation condition. The incident field u^{inc} describes incoming plane waves, i.e.:

$$u^{inc} = e^{-ik(x \cos \alpha + y \sin \alpha)}, \tag{4}$$

in which α is the angle formed between the normal to the traveling wave front and the global x -coordinate axis, and an $e^{i\omega t}$ time factor has been assumed throughout.

3.2 BEM-based forward problem solution

Using boundary integral equations, the solution to the forward problem given by Eqs. 1–3 can be obtained by the following standard integral representations (for a smooth boundary Γ):

$$u^s = \mathfrak{G} \left[\frac{\partial u^s}{\partial n} \right] - \mathfrak{D}[u^s], \quad \text{in } \Omega, \tag{5}$$

where \mathfrak{S} and \mathfrak{D} are the single- and double-layers defined for any smooth function q as:¹

$$\mathfrak{S}[q](\mathbf{x}) = \int_{\Gamma} q(\mathbf{y})G(\mathbf{x}, \mathbf{y}) d\Gamma(\mathbf{y}), \quad \mathbf{x} \in \Omega, \mathbf{y} \in \Gamma, \quad (6)$$

$$\mathfrak{D}[q](\mathbf{x}) = \int_{\Gamma} q(\mathbf{y}) \frac{\partial G(\mathbf{x}, \mathbf{y})}{\partial n_{\mathbf{y}}} d\Gamma(\mathbf{y}), \quad \mathbf{x} \in \Omega, \mathbf{y} \in \Gamma, \quad (7)$$

with $G(z)$ denoting the fundamental solution, or Green’s function, i.e.,

$$G(z) = \frac{i}{4} H_0^{(2)}(kz), \quad (8)$$

where $z = |\mathbf{x} - \mathbf{y}|$ is the distance between a point \mathbf{x} within Ω and a point \mathbf{y} on Γ ; $H_0^{(2)}$ denotes the zeroth order Hankel function of the second kind, and $i = \sqrt{-1}$ is the imaginary unit. Equation 5 provides the scattered field in Ω ; by taking into account the following jump relations,

$$\lim_{\Omega \ni \mathbf{x} \rightarrow \mathbf{x} \in \Gamma} \mathfrak{S}[q](\mathbf{x}) = S[q](\mathbf{x}), \quad \text{or} \quad \mathfrak{S}[q] = S[q], \quad (9)$$

$$\lim_{\Omega \ni \mathbf{x} \rightarrow \mathbf{x} \in \Gamma} \mathfrak{D}[q](\mathbf{x}) = -\frac{1}{2}q(\mathbf{x}) + D[q](\mathbf{x}), \quad \text{or} \quad \mathfrak{D}[q] = -\frac{1}{2}q + D[q], \quad (10)$$

in which

$$S[q](\mathbf{x}) = \int_{\Gamma} q(\mathbf{y})G(\mathbf{x}, \mathbf{y}) d\Gamma(\mathbf{y}), \quad \mathbf{x}, \mathbf{y} \in \Gamma, \quad (11)$$

$$D[q](\mathbf{x}) = \int_{\Gamma} q(\mathbf{y}) \frac{\partial G(\mathbf{x}, \mathbf{y})}{\partial n_{\mathbf{y}}} d\Gamma(\mathbf{y}), \quad \mathbf{x}, \mathbf{y} \in \Gamma, \quad (12)$$

there follows, by taking limits in (5), the classical boundary integral representation:

$$\frac{1}{2}u^s - S \left[\frac{\partial u^s}{\partial n} \right] + D[u^s] = 0, \quad \text{on } \Gamma. \quad (13)$$

The solution of the inverse problem, as it will be shown, entails a number of solutions of the forward problem, each corresponding to a shape perturbation of the boundary Γ ; let us denote with Γ^ξ each such boundary instantiation, implying a dependence on a, yet to be defined, scalar parameter ξ . Then, Eq. 13 provides the basis for the numerical solution of the forward problem, for any boundary instantiation Γ^ξ . We remark that (13) corresponds to the exterior acoustics problem, for which, it is well known (e.g. [24]) that there exists a set of distinct frequencies, corresponding to eigenfrequencies of the interior problem (non-physical), for which (13) becomes singular. A number of schemes to alleviate the

difficulty have been reported [24–26]; though mindful of the difficulty, here we have not implemented any special scheme to address it. In practice, we avoid interrogating frequencies that coincide with the fictitious singular ones.

3.3 The inverse problem

We are concerned with establishing the location of the scatterer S , as well as with describing its boundary Γ . Our problem is driven by measurements at N_s stations (Fig. 1). In such cases, classical lines of investigation suggest the construction of a misfit functional between the measured and computed fields. For example, one candidate choice is:

$$\mathcal{J}_1(\Gamma^\xi; \xi) = \frac{1}{2} \sum_{j=1}^{N_s} \frac{|u^s(\mathbf{x}_j, \xi) - u_m^s(\mathbf{x}_j)|^2}{|u_m^s(\mathbf{x}_j)|^2}, \quad (14)$$

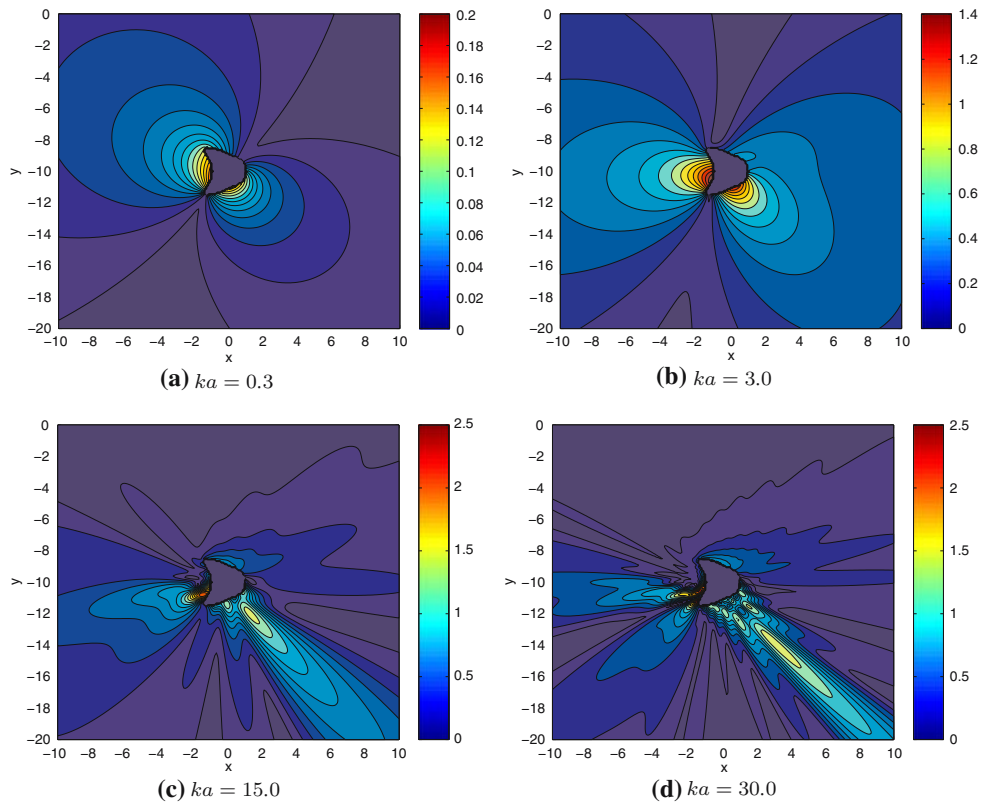
where \mathbf{x}_j denotes the location of the stations. $u_m^s(\mathbf{x})$ is the measured scattered field at \mathbf{x}_j , and $u^s(\mathbf{x}_j, \xi)$ denotes the forward solution computed for some boundary perturbation Γ^ξ , also at the same locations \mathbf{x}_j . \mathcal{J}_1 defines the misfit, in the least-squares sense, of the amplitude of the difference of the complex-valued scattered fields normalized with respect to the measured field, and is a reasonable starting point. However, in a recent article [27], we presented arguments in favor of an amplitude-based misfit functional, defined as:

$$\mathcal{J}(\Gamma^\xi; \xi) = \frac{1}{2} \sum_{j=1}^{N_s} \frac{(|u^s(\mathbf{x}_j, \xi)| - |u_m^s(\mathbf{x}_j)|)^2}{|u_m^s(\mathbf{x}_j)|^2}. \quad (15)$$

In [27], we argued that \mathcal{J}_1 becomes highly oscillatory even for moderate frequencies, presents the optimizer with multiple minima, whose basin of attraction ever narrows as the frequency increases. By contrast, the amplitude-based \mathcal{J} , even though it is missing the enforcement of equality in the phase-angles between the measured and computed fields, is considerably less oscillatory, thereby lending hope that local optimization methods may arrive at the global optimum. Numerical evidence supporting these arguments can be found in [27]. In physical terms, \mathcal{J} exploits the fact that around obstacles embedded in a homogeneous full-space the scattered amplitude distribution is a rather smooth-varying field, as, for example, can be seen in Fig. 2 for the case of a kite-shaped obstacle insonified by plane waves ($\alpha = -45^\circ$) at four different frequencies (this assertion will not be true, in general, for inhomogeneous hosts). With the choice of (15), we seek next the minimization of \mathcal{J} subject to the strong form (1)–(3), written for the domain and boundary perturbations Ω^ξ and Γ^ξ , respectively. Accordingly, we define an augmented functional \mathcal{L} , and seek next to satisfy the first-order optimality conditions. We remark that \mathcal{J} is a linear

¹ We use Euler script letters (e.g. \mathfrak{D}) for domain representations of the layers, i.e. when $\mathbf{x} \in \Omega$, and roman letters (e.g. D) for their boundary counterparts (when $\mathbf{x} \in \Gamma$).

Fig. 2 Scattered pressure amplitude distribution around a kite-shaped rigid scatterer; insonification angle $\alpha = -45^\circ$; multiple frequencies; $a =$ kite height; kite parametrization: $(x(\theta), y(\theta)) = (\cos(\theta) + 0.65(\cos 2\theta - 1), -10 + 1.5 \sin \theta)$, $\theta = 0 \dots 2\pi$. **a** $ka = 0.3$ **b** $ka = 3.0$ **c** $ka = 15.0$ **d** $ka = 30.0$



functional (over the field of real numbers; in Appendix I, we derive the functional’s first variation, needed in Sect. 3.6).

3.4 Augmented functional

The weak imposition of the strong form (1)–(3) via Lagrange multipliers $\lambda(\mathbf{x}^\xi, \xi)$ allows casting the constrained optimization problem as an unconstrained problem and yields the following augmented functional, which we seek to minimize:

$$\begin{aligned} \mathcal{L}(u^s, \lambda, \xi) &= \frac{1}{2} \sum_{j=1}^{N_s} \frac{[|u^s(\mathbf{x}_j, \xi)| - |u_m^s(\mathbf{x}_j)|]^2}{|u_m^s(\mathbf{x}_j)|^2} \\ &+ \text{Re} \left\{ \int_{\Omega^\xi} \lambda(\mathbf{x}^\xi, \xi) [\Delta u^s(\mathbf{x}^\xi, \xi) + k^2 u^s(\mathbf{x}^\xi, \xi)] d\Omega^\xi \right. \\ &- \int_{\Gamma^\xi} \lambda(\mathbf{x}^\xi, \xi) \left[\frac{\partial u^s(\mathbf{x}^\xi, \xi)}{\partial n} + \frac{\partial u^{\text{inc}}(\mathbf{x}^\xi, \xi)}{\partial n} \right] d\Gamma^\xi \\ &\left. - \int_{\Gamma^\infty} \lambda(\mathbf{x}^\xi, \xi) \left[\frac{\partial u^s(\mathbf{x}^\xi, \xi)}{\partial n} - iku^s(\mathbf{x}^\xi, \xi) \right] d\Gamma^\infty \right\}. \end{aligned} \tag{16}$$

In (16), only the real part of the weak imposition of (1)–(3) appears, since this is sufficient for ensuring that the strong form is satisfied, while conveniently allowing for a real-valued

functional, which greatly facilitates the computational process. Seeking the minimization of \mathcal{L} in (16) is tantamount to ensuring, simultaneously, the matching of the measured to the computed response, and the satisfaction of the governing equations for the true shape of the interrogated scatterer. To this end, we seek to satisfy the Karush–Kuhn–Tucker (KKT) first-order optimality conditions [28, 29], by requiring that the variations of \mathcal{L} with respect to λ , u^s , and ξ vanish. However, since here the model parameters amount to parameterizations of boundary shapes Γ^ξ that change during the search iterations, we discuss first the necessary relations for addressing the mathematical details of the subsequent development.

3.5 Total differentiation due to boundary shape evolution

Following the works of Bonnet, Guzina, and Fata [1–4], here too we adopt the concept of a moving boundary to describe the boundary shape evolution between successive updates of the boundary parameterization. In other words, we assume that between shape updates the boundary evolves or moves according to a transformation velocity \mathbf{v} (Fig. 3). Of course, this velocity is fictitious, yet it provides the proper context for computing derivatives and integrals over a domain (Ω) and boundary (Γ) that keep changing as the estimates for the location and shape of the scatterer get updated. In general, the transformation velocity has two components (for a planar curve), one tangential (v_t), and one normal (v_n) to the boundary. It is the imposition of this velocity field on the

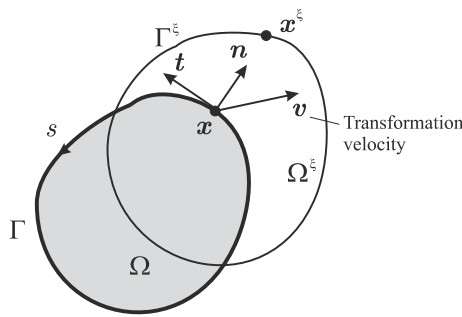


Fig. 3 Boundary shape evolution under a velocity transformation field

boundary that forces the boundary shape to evolve, driven by the optimizer’s enforcing of the underlying physics. Here, we assume that the boundary evolution is due only to the normal velocity component v_n ($v_t \equiv 0$). We remark that this choice is not restrictive, under the assumption of relatively small boundary perturbations (see [30]). The derivatives of integrals and functionals defined on a volume and boundary evolving by means of a scalar parameter were originally provided by Petryk in [30]. We repeat the key expressions below to ease the development.

Let \mathbf{x} be a point on the boundary Γ (Fig. 3). Then, under the action of the velocity field v_n , Γ evolves to Γ^ξ , and \mathbf{x} becomes such that:

$$\Gamma \ni \mathbf{x} \rightarrow \mathbf{x} + \xi v_n(\mathbf{x}) \mathbf{n}(\mathbf{x}) \equiv \mathbf{x}^\xi \in \Gamma^\xi, \tag{17}$$

where, for a given normal velocity field, the scalar parameter ξ is all that is needed to characterize the evolving shape [clearly, from (17), ξ is such that $\xi \equiv 0$ on Γ]. Next, we are concerned with the derivatives (sometimes termed total, or material, or Eulerian, or shape) of a scalar field and the derivatives of line and domain integrals defined over Γ^ξ and Ω^ξ , respectively. Let $f(\mathbf{x}^\xi, \xi)$ denote a scalar field defined over Ω^ξ . Then:

$$\begin{aligned} \left[\frac{Df(\mathbf{x}^\xi, \xi)}{D\xi} \right]_{\xi=0} &= \dot{f}^*(\mathbf{x}, 0) \\ &= \frac{\partial f(\mathbf{x}^\xi, \xi)}{\partial \xi} + \nabla f(\mathbf{x}^\xi, \xi) \cdot \mathbf{v}(\mathbf{x}) = \dot{f} + v_n \frac{\partial f}{\partial n}, \end{aligned} \tag{18}$$

where $\dot{f} = \frac{\partial f}{\partial \xi}$. The total derivatives of integrals over Γ^ξ and Ω^ξ are similarly defined as:

$$\begin{aligned} &\left[\frac{D}{D\xi} \int_{\Gamma^\xi} f(\mathbf{x}^\xi, \xi) d\Gamma^\xi \right]_{\xi=0} \\ &= \int_{\Gamma} \left[\dot{f}^*(\mathbf{x}, 0) + f(\mathbf{x}, 0) \operatorname{div}_s \mathbf{v} \right] d\Gamma \\ &= \int_{\Gamma} \left[\dot{f} + v_n \frac{\partial f}{\partial n} - \kappa f v_n \right] d\Gamma. \end{aligned} \tag{19}$$

In (19), we used $\operatorname{div}_s \mathbf{n} \equiv \mathbf{t} \cdot \frac{\partial \mathbf{n}}{\partial s} = -\kappa$, where κ denotes the curvature of the boundary Γ , div denotes the divergence operator, div_s denotes the boundary or surface divergence operator, \mathbf{t} denotes the unit tangential vector on Γ , and s denotes arclength (Fig. 3). Similarly, it can be shown that:

$$\left[\frac{D}{D\xi} \int_{\Omega^\xi} f(\mathbf{x}^\xi, \xi) d\Omega^\xi \right]_{\xi=0} = \int_{\Omega} \dot{f} d\Omega + \int_{\Gamma} f v_n d\Gamma. \tag{20}$$

3.6 The first-order optimality conditions

We turn next to the computation of the first-order optimality conditions. Specifically, we require that:

$$\begin{Bmatrix} \delta_\lambda \mathcal{L} \\ \delta_{u^s} \mathcal{L} \\ \delta_\xi \mathcal{L} \end{Bmatrix} = \mathbf{0}. \tag{21}$$

Notice that the variation with respect to ξ is equivalent to the variation with respect to the shape perturbation parameters. We derive next the first-order conditions. By taking the variation of \mathcal{L} in (16) with respect to the Lagrange multiplier (or adjoint variable), there results:

$$\begin{aligned} \delta_\lambda \mathcal{L} = \operatorname{Re} \left\{ \int_{\Omega^\xi} \delta \lambda (\Delta u^s + k^2 u^s) d\Omega^\xi \right. \\ \left. - \int_{\Gamma^\xi} \delta \lambda \left(\frac{\partial u^s}{\partial n} + \frac{\partial u^{\operatorname{inc}}}{\partial n} \right) d\Gamma^\xi \right. \\ \left. - \int_{\Gamma^\infty} \delta \lambda \left(\frac{\partial u^s}{\partial n} - i k u^s \right) d\Gamma^\infty \right\}. \end{aligned} \tag{22}$$

Setting $\delta_\lambda \mathcal{L} = 0$ in (22), while taking into account that $\delta \lambda$ is arbitrary, recovers the state problem $\forall \xi$:

State problem:

$$\Delta u^s(\mathbf{x}) + k^2 u^s(\mathbf{x}) = 0, \quad \mathbf{x} \in \Omega^\xi, \tag{23}$$

$$\frac{\partial u^s}{\partial n}(\mathbf{x}) = -\frac{\partial u^{\operatorname{inc}}}{\partial n}(\mathbf{x}), \quad \mathbf{x} \in \Gamma^\xi, \tag{24}$$

$$\lim_{r \rightarrow \infty} \sqrt{r} \left(\frac{\partial u^s}{\partial r} - i k u^s \right) = 0. \tag{25}$$

Similarly, by taking the variation of \mathcal{L} with respect to the state variable, there results:

$$\delta_{u^s} \mathcal{L} = \delta_{u^s} \mathcal{J} + \operatorname{Re} \left\{ \int_{\Omega^\xi} \lambda (\Delta \delta u^s + k^2 \delta u^s) d\Omega^\xi - \int_{\Gamma^\xi} \lambda \frac{\partial \delta u^s}{\partial n} d\Gamma^\xi - \int_{\Gamma^\infty} \lambda \left(\frac{\partial \delta u^s}{\partial n} - ik \delta u^s \right) d\Gamma^\infty \right\}. \tag{26}$$

Using integration by parts for the first integral in (26) yields:

$$\delta_{u^s} \mathcal{L} = \delta_{u^s} \mathcal{J} + \operatorname{Re} \left\{ \int_{\Omega^\xi} (\nabla \cdot (\lambda \nabla \delta u^s) - \nabla \lambda \cdot \nabla \delta u^s + \lambda k^2 \delta u^s) d\Omega^\xi - \int_{\Gamma^\xi} \lambda \frac{\partial \delta u^s}{\partial n} d\Gamma^\xi - \int_{\Gamma^\infty} \lambda \left(\frac{\partial \delta u^s}{\partial n} - ik \delta u^s \right) d\Gamma^\infty \right\}. \tag{27}$$

Using the divergence theorem for the first term of the first integral, and integration by parts for the second term of the same integral yields:

$$\delta_{u^s} \mathcal{L} = \delta_{u^s} \mathcal{J} + \operatorname{Re} \left\{ \int_{\Gamma^\xi} \lambda \frac{\partial \delta u^s}{\partial n} d\Gamma^\xi + \int_{\Gamma^\infty} \lambda \frac{\partial \delta u^s}{\partial n} d\Gamma^\infty + \int_{\Omega^\xi} (\delta u^s \Delta \lambda - \nabla \cdot (\delta u^s \nabla \lambda)) d\Omega^\xi + \int_{\Omega^\xi} \lambda k^2 \delta u^s d\Omega^\xi - \int_{\Gamma^\xi} \lambda \frac{\partial \delta u^s}{\partial n} d\Gamma^\xi - \int_{\Gamma^\infty} \lambda \left(\frac{\partial \delta u^s}{\partial n} - ik \delta u^s \right) d\Gamma^\infty \right\}. \tag{28}$$

Finally, using the divergence theorem for the second term of the third integral of (28), and (62) from Appendix I for the variation of the misfit \mathcal{J} , there results the variation of the augmented functional with respect to the state variable u^s :

$$\delta_{u^s} \mathcal{L} = \operatorname{Re} \left\{ \int_{\Omega^\xi} \sum_{j=1}^{N_s} \delta u^s \frac{\bar{u}^s}{|u_m^s|^2} \left[1 - \frac{|u_m^s|}{|u^s|} \right] \Delta_D d\Omega^\xi + \int_{\Omega^\xi} \delta u^s (\Delta \lambda + k^2 \lambda) d\Omega^\xi + \int_{\Gamma^\xi} \delta u^s \frac{\partial \lambda}{\partial n} d\Gamma^\xi - \int_{\Gamma^\infty} \delta u^s \left(\frac{\partial \lambda}{\partial n} - ik \lambda \right) d\Gamma^\infty \right\}, \tag{29}$$

where an overbar (\bar{u}^s) denotes complex conjugate. Next,

setting $\delta_{u^s} \mathcal{L} = 0$ for arbitrary δu^s recovers the adjoint problem:

Adjoint problem:

$$\Delta \lambda(\mathbf{x}) + k^2 \lambda(\mathbf{x}) = - \sum_{j=1}^{N_s} \frac{\bar{u}^s(\mathbf{x})}{|u_m^s(\mathbf{x}_j)|^2} \left[1 - \frac{|u_m^s(\mathbf{x}_j)|}{|u^s(\mathbf{x})|} \right] \times \Delta_D(\mathbf{x} - \mathbf{x}_j), \quad \mathbf{x} \in \Omega^\xi, \tag{30}$$

$$\frac{\partial \lambda}{\partial n} = 0, \quad \text{on } \Gamma^\xi, \tag{31}$$

$$\lim_{r \rightarrow \infty} \sqrt{r} \left(\frac{\partial \lambda}{\partial r} - ik \lambda \right) = 0. \tag{32}$$

Notice that the adjoint problem is nearly identical to the state problem: the governing operator is the same, however the forcing term in the adjoint problem, provided by the right-hand-side of (30), depends on the state variable u^s at the measurement stations. The boundary condition on the surface of the scatterer is also affected, per (31).

Finally, the variation of \mathcal{L} with respect to ξ results in:

$$\begin{aligned} \delta_\xi \mathcal{L} &= \operatorname{Re} \left[\int_{\Omega} \sum_{j=1}^{N_s} \dot{u}^s \frac{\bar{u}^s}{|u_m^s|^2} \left(1 - \frac{|u_m^s|}{|u^s|} \right) \Delta_D d\Omega \right] \\ &+ \frac{D}{D\xi} \operatorname{Re} \left[\int_{\Omega^\xi} \lambda (\Delta u^s + k^2 u^s) d\Omega^\xi - \int_{\Gamma^\xi} \lambda \left(\frac{\partial u^s}{\partial n} + \frac{\partial u^{\text{inc}}}{\partial n} \right) d\Gamma^\xi - \int_{\Gamma^\infty} \lambda \left(\frac{\partial u^s}{\partial n} - ik u^s \right) d\Gamma^\infty \right]_{\xi=0} \\ &= \operatorname{Re} \left[\int_{\Omega} \sum_{j=1}^{N_s} \dot{u}^s \frac{\bar{u}^s}{|u_m^s|^2} \left(1 - \frac{|u_m^s|}{|u^s|} \right) \Delta_D d\Omega \right] \\ &+ \frac{D}{D\xi} \operatorname{Re} \left[\int_{\Omega^\xi} (-\nabla \lambda \cdot \nabla u^s + k^2 \lambda u^s) d\Omega^\xi - \int_{\Gamma^\xi} \lambda \frac{\partial u^{\text{inc}}}{\partial n} d\Gamma^\xi \right]_{\xi=0}, \tag{33} \end{aligned}$$

where we used:

$$\int_{\Omega^\xi} \nabla \cdot \lambda \nabla u^s d\Omega^\xi = \int_{\Gamma^\xi} \lambda \frac{\partial u^s}{\partial n} d\Gamma^\xi + \int_{\Gamma^\infty} \lambda \frac{\partial u^s}{\partial n} d\Gamma^\infty. \tag{34}$$

Using the total derivative from (20), (33) becomes:²

$$\begin{aligned} \delta_\xi \mathcal{L} = & \operatorname{Re} \left[\int_\Omega \sum_{j=1}^{N_s} \dot{u}^s \frac{\bar{u}^s}{|u_m^s|^2} \left(1 - \frac{|u_m^s|}{|u^s|} \right) \Delta_D \, d\Omega \right] \\ & - \operatorname{Re} \left[\int_\Omega \left(\nabla \dot{\lambda} \cdot \nabla u^s + \nabla \lambda \cdot \nabla \dot{u}^s - k^2 \dot{\lambda} u^s - k^2 \lambda \dot{u}^s \right) d\Omega \right. \\ & + \int_\Gamma \left(\nabla \lambda \cdot \nabla u^s - k^2 \lambda u^s \right) v_n \, d\Gamma \\ & \left. + \frac{D}{D\xi} \left[\int_{\Gamma^\xi} \left(\lambda \frac{\partial u^{\text{inc}}}{\partial n} \right) d\Gamma^\xi \right] \right]_{\xi=0}. \end{aligned} \tag{35}$$

In (35), the last term, using (19), can be expanded as follows:

$$\begin{aligned} & \frac{D}{D\xi} \left[\int_{\Gamma^\xi} \left(\lambda \frac{\partial u^{\text{inc}}}{\partial n} \right) d\Gamma^\xi \right]_{\xi=0} \\ &= \int_\Gamma \left\{ \frac{\partial}{\partial \xi} \left(\lambda \frac{\partial u^{\text{inc}}}{\partial n} \right) + v_n \frac{\partial}{\partial n} \left(\lambda \frac{\partial u^{\text{inc}}}{\partial n} \right) \right. \\ & \quad \left. - \kappa \left(\lambda \frac{\partial u^{\text{inc}}}{\partial n} \right) v_n \right\} d\Gamma \\ &= \int_\Gamma \left\{ \dot{\lambda} \frac{\partial u^{\text{inc}}}{\partial n} + \lambda \frac{\partial}{\partial \xi} \left(\frac{\partial u^{\text{inc}}}{\partial n} \right) + v_n \frac{\partial \lambda}{\partial n} \frac{\partial u^{\text{inc}}}{\partial n} \right. \\ & \quad \left. + v_n \lambda \frac{\partial}{\partial n} \left(\frac{\partial u^{\text{inc}}}{\partial n} \right) - v_n \kappa \lambda \frac{\partial u^{\text{inc}}}{\partial n} \right\} d\Gamma. \end{aligned} \tag{36}$$

In Appendix II, we show that:

$$\frac{\partial}{\partial \xi} \left(\frac{\partial u^{\text{inc}}}{\partial n} \right) = - \frac{\partial u^{\text{inc}}}{\partial s} \frac{\partial v_n}{\partial s} + v_n \frac{\partial u^{\text{inc}}}{\partial s} \operatorname{div} \mathbf{t}. \tag{37}$$

Thus, using (37), first in (36), and then substituting the resulting expression back in (35), yields:

$$\begin{aligned} \delta_\xi \mathcal{L} = & \operatorname{Re} \left[\int_\Omega \sum_{j=1}^{N_s} \dot{u}^s \frac{\bar{u}^s}{|u_m^s|^2} \left(1 - \frac{|u_m^s|}{|u^s|} \right) \Delta_D \, d\Omega \right] \\ & - \operatorname{Re} \left\{ \int_\Omega \left(\nabla \dot{\lambda} \cdot \nabla \dot{u}^s - k^2 \dot{\lambda} u^s \right) d\Omega \right. \\ & + \int_\Omega \left(\nabla \dot{\lambda} \cdot \nabla u^s - k^2 \dot{\lambda} u^s \right) d\Omega + \int_\Gamma \dot{\lambda} \frac{\partial u^{\text{inc}}}{\partial n} \, d\Gamma \\ & \left. + \int_\Gamma \left(\nabla \lambda \cdot \nabla u^s - k^2 \lambda u^s \right) v_n \, d\Gamma \right\} \end{aligned}$$

² On physical grounds, neither λ nor u^s on Γ^∞ depend on ξ , and thus $\frac{D}{D\xi} [\int_{\Gamma^\infty} \lambda u^s d\Gamma^\infty]_{\xi=0} = 0$, and thus the term is henceforth omitted.

$$\begin{aligned} & - \int_\Gamma \lambda \frac{\partial u^{\text{inc}}}{\partial s} \frac{\partial v_n}{\partial s} \, d\Gamma + \int_\Gamma v_n \lambda \frac{\partial u^{\text{inc}}}{\partial n} \operatorname{div} \mathbf{t} \, d\Gamma \\ & + \int_\Gamma v_n \frac{\partial \lambda}{\partial n} \frac{\partial u^{\text{inc}}}{\partial n} \, d\Gamma + \int_\Gamma v_n \lambda \frac{\partial}{\partial n} \left(\frac{\partial u^{\text{inc}}}{\partial n} \right) \, d\Gamma \\ & - \int_\Gamma v_n \kappa \lambda \frac{\partial u^{\text{inc}}}{\partial n} \, d\Gamma \}. \end{aligned} \tag{38}$$

The first two terms in (38) constitute a weak form of the adjoint problem (30) with \dot{u}_s as a weight function, and they, thus, vanish. Similarly, the third and fourth terms in (38) constitute a weak form of the state problem (23) with $\dot{\lambda}$ as a weight function, and, thus, they too cancel out. Owing to (31), the eighth term vanishes, and the following expression admits the simplification:

$$\nabla \lambda \cdot \nabla u^s = \frac{\partial \lambda}{\partial s} \frac{\partial u^s}{\partial s} \quad \text{on } \Gamma. \tag{39}$$

Using (39), (38) reduces to:³

$$\begin{aligned} \delta_\xi \mathcal{L} = & \operatorname{Re} \int_\Gamma v_n \left[- \frac{\partial \lambda}{\partial s} \frac{\partial (u^s + u^{\text{inc}})}{\partial s} - \lambda \frac{\partial u^{\text{inc}}}{\partial s} \operatorname{div} \mathbf{t} \right. \\ & \left. + k^2 \lambda (u^s + u^{\text{inc}}) \right] d\Gamma. \end{aligned} \tag{40}$$

Equation (40) vanishes only when the assumed boundary Γ coincides with the true boundary (or a local minimum). For an assumed boundary, the state u^s and adjoint variables λ satisfying the first and second optimality conditions can be obtained by solving the state and adjoint problems (23)–(25), and (30)–(32), respectively. Therefore, the optimization process is equivalent to finding the boundary that forces (40) to vanish with the previously computed state and adjoint variables. This gives rise to the control problem:

Control problem:

$$\begin{aligned} & \operatorname{Re} \int_\Gamma v_n \left[- \frac{\partial \lambda}{\partial s} \frac{\partial (u^s + u^{\text{inc}})}{\partial s} - \lambda \frac{\partial u^{\text{inc}}}{\partial s} \operatorname{div} \mathbf{t} \right. \\ & \quad \left. + k^2 \lambda (u^s + u^{\text{inc}}) \right] d\Gamma = 0. \end{aligned} \tag{41}$$

4 Inversion process

In this section, we discuss the numerical implementation of a reduced-space method for the solution of the inverse shape detection and localization problem. Specifically, the focus is on the solution of the state (23)–(25), the adjoint (30)–(32),

³ We also took into account that u^{inc} satisfies the Helmholtz equation and therefore: $\frac{\partial^2 u^{\text{inc}}}{\partial n^2} = \kappa \frac{\partial u^{\text{inc}}}{\partial n} - \frac{\partial^2 u^{\text{inc}}}{\partial s^2} - k^2 u^{\text{inc}}$.

and the control problem (41). In principle, all three problems could be solved simultaneously (a full-space method) for the unknown state variables, adjoint variables, and model parameters. To avoid the increased computational cost, we opt for a reduced-space method, whereby the state and adjoint variables are eliminated first. To solve the state and adjoint problems, any numerical method (finite differences, finite elements, boundary elements, etc.) can be used; here we favor the boundary element method, for the benefit that it provides with the automatic satisfaction of the radiation condition, and for the dimensionality reduction that it affords for discretization purposes (only Γ needs to be discretized). Accordingly, the state problem (23)–(25) is tantamount (as discussed in Sect. 3.2) to the following boundary integral equation:

$$\frac{1}{2}u^s + D[u^s] = -S\left[\frac{\partial u^{\text{inc}}}{\partial n}\right], \quad \text{on } \Gamma. \quad (42)$$

Similarly, the boundary integral equation for the adjoint problem (30)–(32) can be written as:

$$\begin{aligned} \frac{1}{2}\lambda + D[\lambda] = & -\sum_{j=1}^{N_s} G(\mathbf{x}, \mathbf{x}_j) \frac{\bar{u}^s(\mathbf{x}_j)}{|u_m^s(\mathbf{x}_j)|^2} \\ & \times \left(1 - \frac{|u_m^s(\mathbf{x}_j)|}{|u^s(\mathbf{x}_j)|}\right), \quad \text{on } \Gamma. \end{aligned} \quad (43)$$

Notice that the single-layer term $S\left[\frac{\partial \lambda}{\partial n}\right]$ vanishes for the adjoint variable by virtue of (31). Equations (42) and (43) are discretized per the standard procedures of the boundary element method; here we use quadratic isoparametric elements. Notice further, that the left-hand-side operators of both integral equations are the same: only a *single* system matrix inversion is needed for both problems.

For every estimate (and description) Γ^ξ of Γ , first (42) is solved to return u^s on Γ^ξ ; notice that the forcing term on the right-hand-side of (43) depends on the incoming wave u^{inc} . Once u^s is obtained, the forcing term on the right-hand-side of (43) is completely defined, and thus, (43) can be solved to return the adjoint variable λ , also on Γ^ξ . Both of these steps would satisfy the first two optimality conditions.

There are many approaches to ensure the satisfaction of the third optimality condition (41); here we reason as follows: once, for an assumed shape, the state problem has been solved, then the side constraints in (16) vanish, and thus the minimization of the augmented functional \mathcal{L} is tantamount to the minimization of the misfit functional \mathcal{J} . Therefore, with the proviso of the satisfaction of the state problem, there also holds that:

$$\delta_{p_i} \mathcal{L} = \nabla_{p_i} \mathcal{J}, \quad (44)$$

where p_i denotes the i th model parameter (unknown).

However, from (40), it follows that:

$$\begin{aligned} \delta_{p_i} \mathcal{L} = \text{Re} \int_{\Gamma} v_n^i \left[-\frac{\partial \lambda}{\partial s} \frac{\partial (u^s + u^{\text{inc}})}{\partial s} - \lambda \frac{\partial u^{\text{inc}}}{\partial s} \text{div} \mathbf{t} \right. \\ \left. + k^2 \lambda (u^s + u^{\text{inc}}) \right] d\Gamma, \end{aligned} \quad (45)$$

where v_n^i denotes the velocity corresponding to the i th model parameter. Therefore, if we now seek to minimize the original misfit \mathcal{J} , using, for example, a conjugate-gradient (CG) scheme, the components of the gradient of the misfit are readily given by (45), while at the same time both the state and adjoint problems would have been satisfied. Thus, all that remains is to define the components of the transformation velocity. To this end, let $\Psi(\mathbf{p})$ denote the (vector) function describing the parameterization of the unknown boundary, in terms of a finite set of unknown model parameters \mathbf{p} . Then, the transformation velocity at a point $\mathbf{x} \in \Gamma$ is defined as:

$$v_n^i(\mathbf{x}) = \frac{\partial \Psi(\mathbf{p})}{\partial p_i} \Big|_{\mathbf{x}} \cdot \mathbf{n}(\mathbf{x}). \quad (46)$$

Consequently, the components of the gradient of the misfit functional \mathcal{J} that are needed for the CG (or any other gradient-based scheme) are given as:

$$\begin{aligned} \nabla_{p_i} \mathcal{J} = \text{Re} \int_{\Gamma} \left[\frac{\partial \Psi_x}{\partial p_i} n_x + \frac{\partial \Psi_y}{\partial p_i} n_y \right] \\ \times \left[-\frac{\partial \lambda}{\partial s} \frac{\partial (u^s + u^{\text{inc}})}{\partial s} + \lambda \frac{\partial u^{\text{inc}}}{\partial s} \left(\frac{\partial n_y}{\partial x} - \frac{\partial n_x}{\partial y} \right) \right. \\ \left. + k^2 \lambda (u^s + u^{\text{inc}}) \right] d\Gamma, \end{aligned} \quad (47)$$

where Ψ_x and Ψ_y are the cartesian components of the parameterization function Ψ , and n_x, n_y are similarly the components of the normal vector. In our implementation we use a Polak-Ribière CG scheme with the following termination criterion:

$$\frac{2|\mathcal{J}_{\text{previous}} - \mathcal{J}_{\text{current}}|}{|\mathcal{J}_{\text{previous}}| + |\mathcal{J}_{\text{current}}| + \epsilon} < \text{TOL}, \quad (48)$$

where ϵ is a small positive number, and TOL is a user-controllable tolerance, and $\mathcal{J}_{\text{previous, current}}$ refer to previous and current shape iteration calculations of the misfit \mathcal{J} , respectively (we typically set TOL and ϵ to 10^{-8}). We remark that during each search iteration, the state and adjoint problems are each solved once, in order to allow computation of the misfit's gradient.

4.1 Frequency-continuation scheme

One of the difficulties of wavefield-based inversion is associated with the presence of multiple local minima due to

the highly oscillatory nature of the misfit functionals. To improve the chances of the described procedure to converge we employ continuation schemes. Clearly, even if convergence is achieved for a single frequency and a single wave direction, there is no guarantee that the converged model parameters correspond to the true scatterer location and shape. In addition, at high probing frequencies, the initial estimates have to be quite close to the target ones, since there are multiple attraction basins that are quite narrow. Our motivation for embracing continuation schemes stems from physical and technological grounds, recognizing that contemporary probing devices have considerable frequency and directionality agility. The key idea behind continuation schemes is to employ a sequence of seemingly uncoupled problems, whereby the converged model parameters from one problem are fed as initial guesses to the next, and so forth, until all problems converge under the *same* set of model parameters; details can be found in [27]. There are at least three forms the continuation scheme may take in the shape detection and localization problem: (i) continuation over multiple probing wave frequencies, (ii) continuation over multiple incidence angles, and (iii) continuation over multiple probing wave frequencies and directions. Algorithm 1 captures tersely the continuation scheme, when multiple frequencies are used (extensions to accommodate multiple probing directions or combination of directions and frequencies are straightforward).

The algorithm, as sketched, is concerned with a series of decoupled inverse problems, that is, one problem for each frequency (even at multiple wave incidence angles), even though the scatterer is the same. The coupling of all these problems is a loose one: it is achieved through the revisiting of the misfit functional values for all frequencies at the end of the process to ensure that the final set of converged model parameters satisfies all problems (steps 10–17 in Algorithm 1). In practice, we apply the continuation scheme by starting with a low probing frequency and increase the frequency until convergence. Our numerical results indicate that a few frequencies (three to four) are typically sufficient for resolving the shape and localization problem. It is noteworthy that low probing frequencies typically allow for the resolution of location, rather than the shape, whereas higher frequencies fine-tune the shape without affecting the location.

5 Numerical experiments

In this section we examine the performance of the proposed scheme via numerical experiments, and report on the results. In all example problems, the measured scattered pressures are synthesized numerically by solving the forward problem using the boundary element method with a mesh different from the one we use in the inversion process in order to

avoid committing a classical “inverse crime.” Throughout, we assume that convergence to a set of model parameters describing the sought object has been attained when criterion (48) has been met.

Algorithm 1 Frequency-continuation scheme

```

1: Set InitialModelParameters
2: Set ModelParameters = InitialModelParameters
3: for all Frequencies do
4:   Set ith-Frequency
5:   Use ModelParameters
6:   Single-Frequency-Direction CG Algorithm
     (Save ith-Misfit)
     (Save ConvergedModelParameters)
7:   Set ModelParameters = ConvergedModelParameters
8: end for
9: Set LastModelParameters = ConvergedModelParameters
10: for all Frequencies do
11:   Compute Misfit (Use LastModelParameters)
12:   if Misfit ≤ ith-Misfit then
13:     Converged
14:   else
15:     Failed; Exit
16:   end if
17: end for

```

5.1 Example I: circular scatterer

We begin with a simple example problem in which we have a priori information that the unknown obstacle is of circular shape. Accordingly, the location and the size of the obstacle is defined by three unknown parameters: the center’s coordinates x_0 and y_0 , and the radius R . The boundary parameterization function is cast as:

$$\Psi(\mathbf{p}) = \begin{Bmatrix} x \\ y \end{Bmatrix} = \begin{Bmatrix} x_0 + R \cos \theta \\ y_0 + R \sin \theta \end{Bmatrix}, \tag{49}$$

where θ ranges from 0 to 2π , and $\mathbf{p} = [x_0, y_0, R]^T$. The true obstacle is centered at $(0, -10)$, and has unit radius. We start the search process with a circle of radius 3, centered at $(15, -20)$. We use a plane wave with an incidence angle $\alpha = -45^\circ$. We measure the response at three observation stations located at $(-10, 0)$, $(0, 0)$ and $(10, 0)$. The configuration of the problem is depicted in Fig. 4.

We use both the single-frequency and the frequency-continuation scheme to resolve the shape. For the single-frequency scheme, we use an incident wave with a wave number $k = 0.1$ and $TOL = 10^{-8}$. To illustrate the effects of the frequency-continuation scheme, we use three frequencies corresponding to $k = 0.1, 1.0$, and 2.0 and set TOL to 10^{-2} . The convergence patterns of the unknown parameters using the single-frequency and the frequency-continuation scheme are shown in Fig. 5; the results are summarized in Table 1 and the path to convergence when the frequency-continuation scheme is used is depicted in Fig. 6.

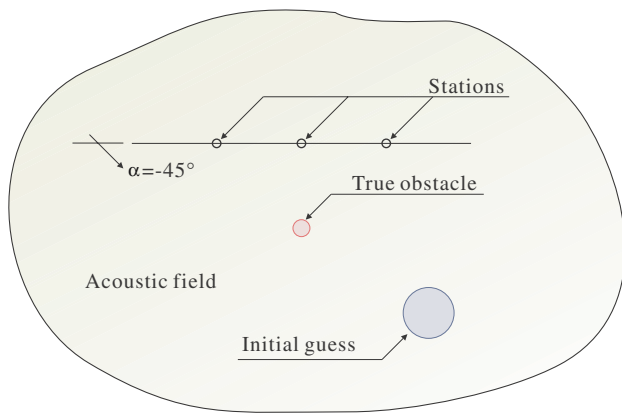


Fig. 4 Example I configuration—circular scatterer

As it can be seen in Fig. 5, all three parameters converge to the target values under both the single-frequency scheme and the frequency-continuation scheme. Notice that the set tolerance is, by design, different between the single-frequency and frequency-continuation schemes: for example, for $TOL=10^{-2}$, when $k = 0.1$ the inversion procedure terminates at the 3rd iteration [criterion (48) has been met] with the “converged” values as shown in Table 1. Similarly for $k = 1.0$. When the set tolerance is decreased to ($TOL=10^{-8}$) (single-frequency case), then the iterations continue until convergence in the 69th iteration. We remark that in both cases the model parameters are near identical.⁴ Thus, when the frequency-continuation scheme is used, convergence is faster (Fig. 5). Furthermore, we note that the convergence to the true obstacle failed when the single-frequency scheme was used with a higher frequency ($k = 2.0$). It is also noteworthy that when, instead of using the amplitude-based misfit functional, we used \mathcal{J}_1 [defined in (14)], convergence to the true scatterer failed for the same initial guess and overall configuration; convergence was possible only when the initial guess came very close to the target. Thus far, these results lend support to the claim that the combination of the amplitude-based misfit functional with the frequency-continuation scheme alleviate the difficulties associated with the solution multiplicity.

5.2 Example II: penny-shaped scatterer

Next, we examine the performance of the proposed scheme using a penny-shaped scatterer. To realize the penny-shaped scatterer, we used an ellipse whose ratio of the minor axis length (b) to the major axis length (a) is 1/10. The center coordinate (x_0, y_0) of the true scatterer is at $(0, -10)$, and

⁴ Single-frequency scheme: $x_0 = 1.0453 \times 10^{-5}$, $y_0 = -10.00002$, $R = 0.99999$; frequency-continuation: $x_0 = 1.3726 \times 10^{-5}$, $y_0 = -9.99999$, $R = 0.99999$.

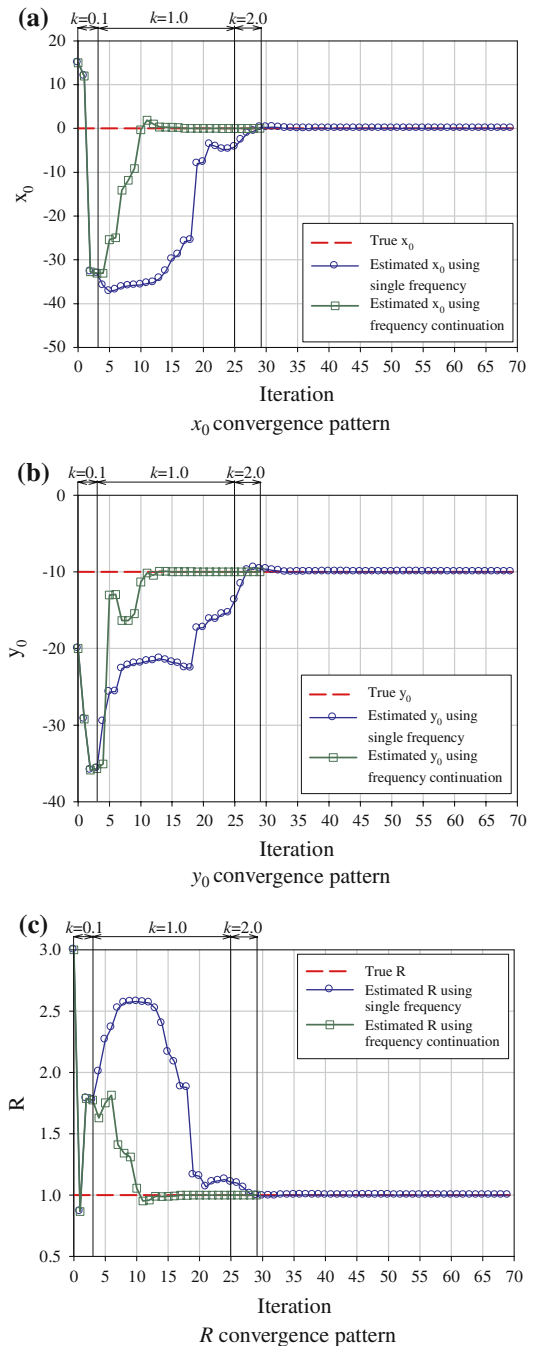


Fig. 5 Convergence patterns of the model parameters of a circular scatterer using a single-frequency and a frequency-continuation scheme. **a** x_0 convergence pattern **b** y_0 convergence pattern. **c** R convergence pattern

the length of the major semi-axis (a) and minor semi-axis (b) are 1.5 and 0.15, respectively. Accordingly, the boundary parameterization function is cast as:

$$\Psi(p) = \begin{Bmatrix} x \\ y \end{Bmatrix} = \begin{Bmatrix} x_0 + a \cos \theta \\ y_0 + b \sin \theta \end{Bmatrix}, \tag{50}$$

Table 1 Example I estimated parameters

	x_0	y_0	R
Initial values	15.000	-20.000	3.000
Frequency continuation scheme			
3rd iteration ($k = 0.1$)	-33.063	-35.668	1.775
25th iteration ($k = 1.0$)	-0.001	-10.000	1.000
29th iteration ($k = 2.0$)	0.000	-10.000	1.000
Single frequency scheme			
29th iteration ($k = 0.1$)	0.241	-9.631	0.997
69th iteration ($k = 0.1$)	0.000	-10.000	1.000
Target values	0.000	-10.000	1.000

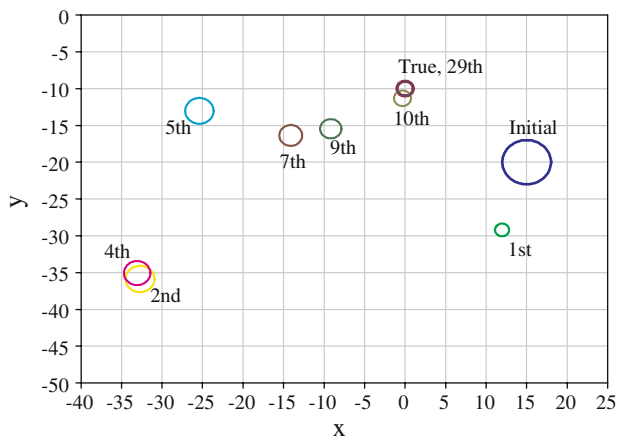


Fig. 6 Convergence path of a circular scatterer using the frequency-continuation scheme

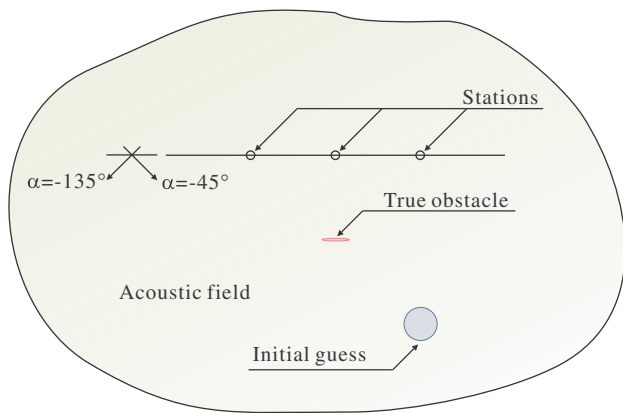


Fig. 7 Example II configuration—penny-shaped scatterer

where θ ranges from 0 to 2π , and $\mathbf{p} = [x_0, y_0, a, b]^T$. We use two probing waves at incidence angles $\alpha = -45^\circ, -135^\circ$; the scattered pressure is measured at three stations located at $(-10, 0), (0, 0)$ and $(10, 0)$. The configuration of the problem is depicted in Fig. 7.

We used a frequency-continuation scheme, where the insonification frequencies were set at $k = 0.1, 1.0$, and 2.0

Table 2 Example II estimated model parameters

Iteration No.	x_0	y_0	a	b
Initial values	1.00e+1	-2.00e+1	2.00e+0	2.00e+0
10th ($k = 0.1$)	-1.59e+0	-1.12e+1	1.34e+0	3.32e-1
20th ($k = 1.0$)	2.03e-3	-9.93e+0	1.48e+0	1.93e-1
60th ($k = 2.0$)	3.63e-8	-1.00e+1	1.50e+0	1.50e-1
Target values	0.00e+0	-1.00e+1	1.50e+0	1.50e-1

(TOL = 10^{-8}). The convergence patterns of the four model parameters are shown in Fig. 8 and the results are summarized in Table 2. The final parameter values obtained using the frequency-continuation scheme are $(3.631 \times 10^{-8}, -10.000, 1.500, 0.1500)$, which are quite close to the true ones $(0, -10, 1.5, 0.15)$. It can be seen that the frequency-continuation scheme yields more accurate estimates than the single-frequency scheme, which, for the low frequency of $k = 0.1$, resulted in converged values of $(-1.594, -11.200, 1.343,$

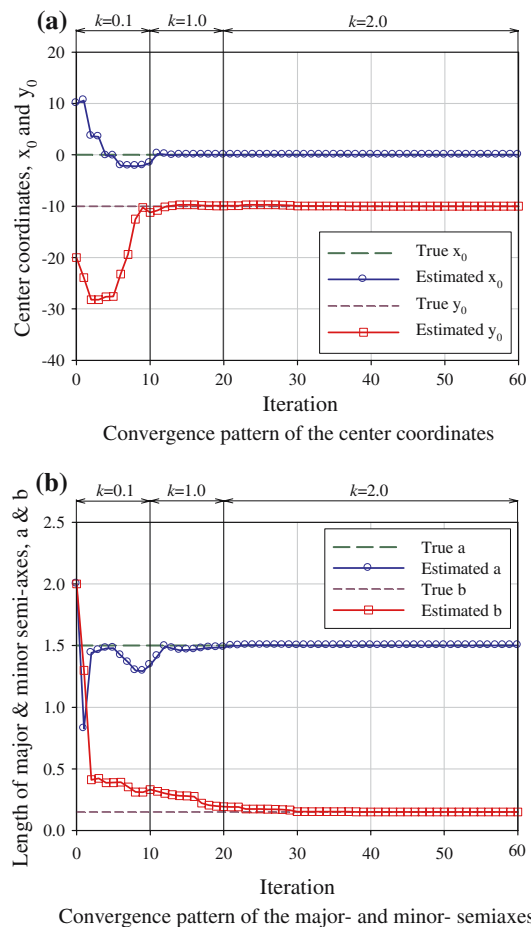


Fig. 8 Convergence patterns of the model parameters of a penny-shaped scatterer using the frequency-continuation scheme. **a** Convergence pattern of the center coordinates. **b** Convergence pattern of the major- and minor-semi axes

0.332). Notice that, by contrast to Example I, here the single-frequency scheme fails to converge for a low frequency and a low tolerance. Clearly, as the frequency increases, the solutions come closer to the true values. Again, if the process were to start at a higher frequency (e.g. $k = 2.0$), the solution would diverge due to the optimizer becoming trapped in a local minimum. It appears important that the frequency initiating the continuation-scheme is a low one. Figure 9 depicts the convergence path to the true penny-shaped scatterer.

5.3 Example III: kite-shaped scatterer

We discuss next one of the most severe inverse scattering tests treated in the literature [20,31,32]: a kite-shaped scatterer whose non-convex parts greatly complicate the reconstruction process (Fig. 10; see also Fig. 2).

The true shape is defined by:

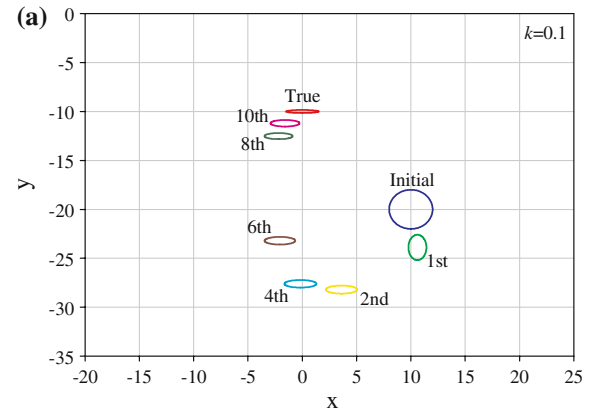
$$x(\theta) = \cos \theta + 0.65 (\cos 2\theta - 1), \tag{51}$$

$$y(\theta) = 1.5 \sin \theta - 10, \tag{52}$$

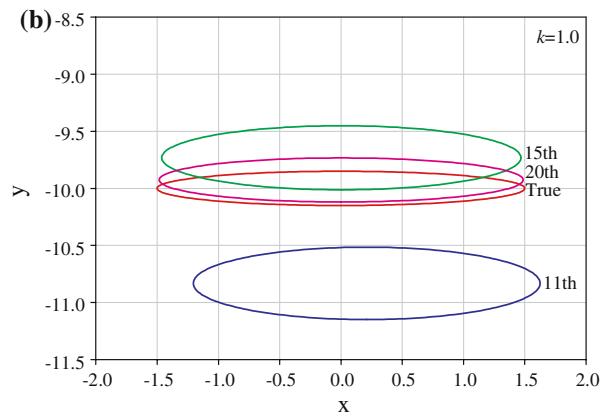
where θ ranges from 0 to 2π . In order to resolve the true shape, we use three incident waves at angles of $-45^\circ, -90^\circ$, and -135° . In addition, the scattered pressure is measured at five stations located at $(-20, 0), (-5, 0), (0, 0), (5, 0)$, and $(20, 0)$, all in the backscattered region. We use $k = 0.1$ and $k = 0.5$ for the frequency-continuation scheme. In order to approximate the boundary, the following boundary parameterization function is employed:

$$\Psi(\mathbf{p}) = \begin{Bmatrix} x \\ y \end{Bmatrix} = \begin{Bmatrix} a_{17} \\ a_{18} \\ a_0 + \sum_{i=1}^8 \{a_{2i-1} \cos(i\theta) + a_{2i} \sin(i\theta)\} \cos \theta \\ a_0 + \sum_{i=1}^8 \{a_{2i-1} \cos(i\theta) + a_{2i} \sin(i\theta)\} \sin \theta \end{Bmatrix}, \tag{53}$$

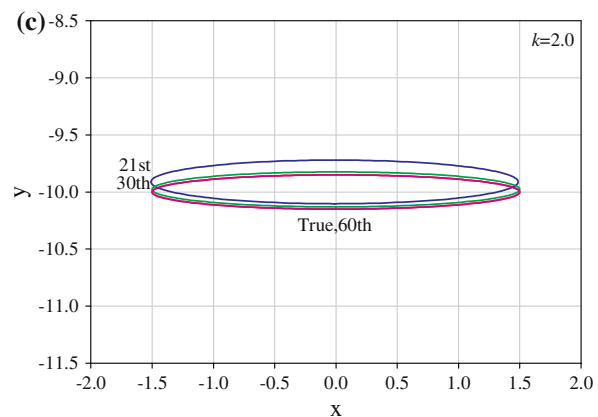
where θ ranges from 0 to 2π , and $\mathbf{p} = [a_0 \dots a_{18}]^T$. Figure 11 depicts the convergence path. Figure 11a is the convergence path for $k = 0.1$; in this case, the solution converged at the 14th iteration; however, as shown in the figure, the shape is still far from the true one. In the next step, the wavenumber is increased to $k = 0.5$, and, per the continuation scheme, the minimization process started from the converged solution of the previous wavenumber. The results from the second wavenumber are shown in Fig. 11b.



Convergence path of penny-shaped scatterer using $k=0.1$



Convergence path of penny-shaped scatterer using $k=1.0$



Convergence path of penny-shaped scatterer using $k=2.0$

Fig. 9 Convergence path of a penny-shaped scatterer using the frequency-continuation scheme. **a** Convergence path of penny-shaped scatterer using $k = 0.1$. **b** Convergence path of penny-shaped scatterer using $k = 1.0$. **c** Convergence path of penny-shaped scatterer using $k = 2.0$

As it can be seen in the figure, convergence is attained (Table 3).

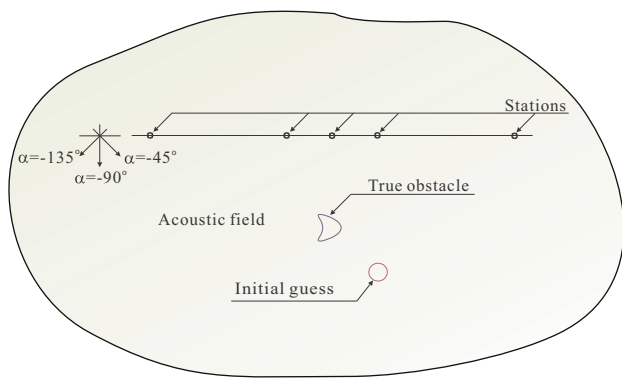


Fig. 10 Example III configuration: kite-shaped scatterer

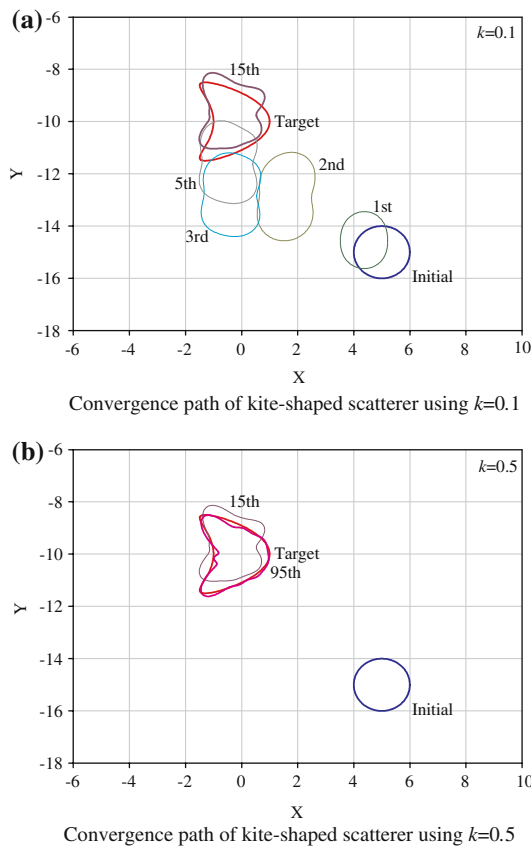


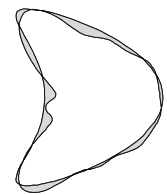
Fig. 11 Convergence path of a kite-shaped scatterer using the frequency-continuation scheme. **a** Convergence path of kite-shaped scatterer using $k = 0.1$. **b** Convergence path of kite-shaped scatterer using $k = 0.5$

We also judge solution fitness by computing the area delineated by the mismatch between the exact and computed boundary shapes (shaded area in Fig. 12), normalized by the total area of the true scatterer. For the kite-shaped scatterer, this fitness metric is 0.4613 and 0.1138, for the 15th and 95th iterations, respectively. Though, the latter indicates an

Table 3 Example III estimated model parameters

i	Initial a_i	15th iteration ($k = 0.1$)	95th iteration ($k = 0.5$)
0	1.0	1.227	1.172
1	0.0	-0.049	-0.034
2	0.0	0.060	0.107
3	0.0	-0.217	-0.151
4	0.0	0.024	0.043
5	0.0	0.146	0.312
6	0.0	-0.037	-0.040
7	0.0	-0.187	-0.189
8	0.0	0.072	0.046
9	0.0	-0.057	0.012
10	0.0	-0.036	-0.023
11	0.0	0.002	0.083
12	0.0	-0.039	-0.014
13	0.0	0.037	-0.109
14	0.0	0.031	0.030
15	0.0	-0.009	0.063
16	0.0	-0.028	-0.028
17	5.0	-0.313	-0.192
18	-15.0	-9.764	-10.183

Fig. 12 Example III—shape mismatch at the 95th iteration



error of about 11%, we expect the fitness to be improved given additional incidences at angles different than the ones we already considered, which will assist in illuminating the non-convex kite zone.

5.4 Example IV: arbitrarily-shaped scatterer

In the previous examples we approximated the boundary by the parameterization function using a relatively small number of parameters. In this example, we seek the boundary by directly inverting for the nodal coordinates which are used in the boundary element discretization for solving both the forward and adjoint problems. We use a potato-shaped scatterer, five recording stations, and three incident waves at angles of -45° , -90° and -135° . The configuration of this problem is depicted in Fig. 13, and the exact shape definition of the sought scatterer is given by:

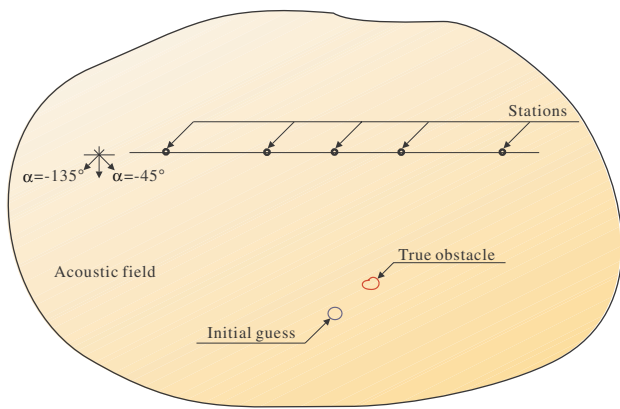
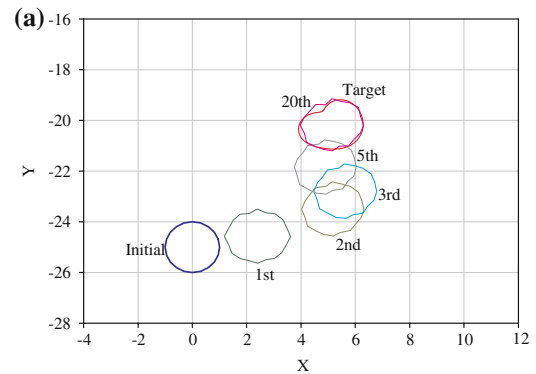


Fig. 13 Example IV configuration—arbitrarily-shaped scatterer

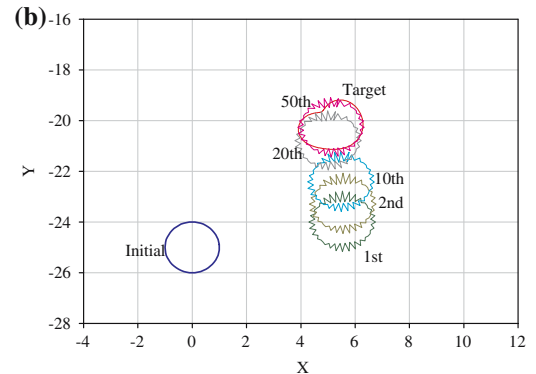
$$\begin{aligned} \begin{Bmatrix} x(\theta) \\ y(\theta) \end{Bmatrix} &= \begin{Bmatrix} a_7 \\ a_8 \end{Bmatrix} \\ &+ \begin{Bmatrix} a_0 + \sum_{i=1}^3 \{a_{2i-1} \cos(i\theta) + a_{2i} \sin(i\theta)\} \cos \theta \\ a_0 + \sum_{i=1}^3 \{a_{2i-1} \cos(i\theta) + a_{2i} \sin(i\theta)\} \sin \theta \end{Bmatrix} \end{aligned} \quad (54)$$

where $[a_0, \dots, a_8]^T = [1, 0.2, -0.3, 0.125, 0.125, -0.05, -0.05, 5, -20]^T$, and $\theta = 0 \dots 2\pi$. We resolve this problem using a single-frequency ($k = 0.1$) and two different boundary discretizations. First, we discretize the boundary using 10 quadratic boundary elements, which implies 20 nodes and a total of 40 parameters (for x and y). Notice that, in this case, the discretization is not fine enough to obtain accurate solutions. Then, we also resolve the same problem using a finer mesh, with 80 nodes and a total of 160 inversion parameters. The results of these two cases are presented in Fig. 14. As shown in Fig. 14a, the solution converges to the target one quite closely even though the discretization is not fine enough. However, in the case of the fine mesh (Fig. 14b), it is observed that the estimated boundaries form a sawtooth shape and the final solution is less accurate than that of the previous case. When using nodal coordinates as inversion variables, we need to guarantee boundary smoothness in the form of an additional penalty in the augmented functional. A candidate form includes a Tikhonov-like penalty on the boundary curvature, as in:

$$R_k \int_{\Gamma} \nabla \kappa \cdot \nabla \kappa \, d\Gamma. \quad (55)$$



Convergence path of arbitrarily-shaped scatterer using 20 nodes



Convergence path of arbitrarily-shaped scatterer using 100 nodes

Fig. 14 Convergence path of arbitrarily-shaped scatterer. **a** Convergence path of arbitrarily-shaped scatterer using 20 nodes. **b** Convergence path of arbitrarily-shaped scatterer using 100 nodes

Furthermore, it is also required that self-intersecting shapes be rejected. These algorithmic features have not been implemented.

6 Conclusions

We have discussed a systematic framework for localizing a scatterer and detecting its shape when embedded in a homogeneous host. The methodology is based on a PDE-constrained optimization approach, endowed with boundary integral equations for the resolution of the ensuing state, adjoint, and control problems that, in turn, ensure the satisfaction of the first-order optimality conditions.

Our main observations are:

- To improve on solution feasibility, we adopted an amplitude-based misfit functional and embedded the inversion process within a frequency- and directionality-continuation scheme. The benefits are twofold: first the misfit functional is less oscillatory, and thus presents fewer and farther-apart spaced local minima, than if one were to consider the complex-valued misfit. Secondly, the continuation scheme enforces convergence over a number of frequencies and/or incident wave directions.

- A low probing frequency seems to enlarge the attraction basin, and as a result, the frequency-continuation scheme with a low initial frequency of the interrogating wave greatly improves performance. Typically, in our experiments, low frequencies localize the scatterer, whereas higher frequencies refine the shape.
- The continuation schemes improve the convergence rate. Even when a low initial frequency is used to widen the attraction basin, the convergence rate in the region near the optimum is slow since the slope of the misfit functional is too flat at the low frequency. Therefore, gradual increase of the insonified wave’s frequency helps to accelerate the convergence rate.
- We have also observed, though not supported by the examples reported herein, that the frequency-continuation scheme yields more accurate estimates than a single-frequency scheme, when both schemes converge. Increasing the frequency of the insonified wave results in a perceived increase of the misfit functional’s slope in the neighborhood of the optimum, thereby accelerating convergence and improving solution accuracy.

7 Appendix I: on the first variation of \mathcal{J} (15)

In (15) we defined the misfit functional as the normalized amplitude-based difference between measured and computed responses. In the following, for brevity, we omit the normalization term, which is always a non-zero positive scalar. We recast (15) as:

$$\begin{aligned} & \frac{1}{2} \sum_{j=1}^{N_s} (|u^s(\mathbf{x}_j)| - |u_m^s(\mathbf{x}_j)|)^2 \\ &= \sum_{j=1}^{N_s} \frac{1}{2} \int_{\Omega} (|u^s(\mathbf{x})| - |u_m^s(\mathbf{x}_j)|)^2 \Delta_D(\mathbf{x} - \mathbf{x}_j) \, d\Omega(\mathbf{x}), \end{aligned} \tag{56}$$

where Δ_D denotes the two-dimensional Dirac function. We seek next the first variation of a single component of the summation in (56), i.e., we seek the first variation of \mathcal{I} , where:

$$\mathcal{I}(u^s) = \frac{1}{2} \int_{\Omega} (|u^s(\mathbf{x})| - |\alpha(\mathbf{x}_0)|)^2 \Delta_D(\mathbf{x} - \mathbf{x}_0) \, d\Omega(\mathbf{x}). \tag{57}$$

Clearly \mathcal{I} is real-valued; formally, $\mathcal{I} : C_b(\mathbb{R}^2, \mathbb{C}) \rightarrow \mathbb{R}$, where C_b denotes the set of continuous, bounded, complex-valued functions on \mathbb{R}^2 over the field of real numbers. Let $\Delta\mathcal{I}$ be the functional increment defined by:

$$\Delta\mathcal{I}(\delta u^s) = \mathcal{I}(u^s + \delta u^s) - \mathcal{I}(u^s), \tag{58}$$

where $\delta u^s(\mathbf{x})$ is the complex-valued increment. Then, it can be shown that:

$$\begin{aligned} & \Delta\mathcal{I}(\delta u^s) \\ &= \frac{1}{2} \int_{\Omega} [u^s(\mathbf{x})\overline{\delta u^s(\mathbf{x})} + \overline{u^s(\mathbf{x})}\delta u^s(\mathbf{x})] \\ & \quad \times \left[1 - \frac{|\alpha(\mathbf{x}_0)|}{|u^s(\mathbf{x})|} \right] \Delta_D(\mathbf{x} - \mathbf{x}_0) \, d\Omega(\mathbf{x}) \\ & \quad + \frac{1}{2} \int_{\Omega} \left[1 - \frac{|\alpha(\mathbf{x}_0)|}{|u^s(\mathbf{x})|} \right] |\delta u^s(\mathbf{x})|^2 \Delta_D(\mathbf{x} - \mathbf{x}_0) \, d\Omega(\mathbf{x}) \\ &= \Phi(\delta u^s) + \mathcal{R}(\delta u^s), \end{aligned} \tag{59}$$

where $\lim_{\|\delta u^s\| \rightarrow 0} \mathcal{R}(\delta u^s) = 0$, and the functional Φ is defined as:

$$\begin{aligned} \Phi(\delta u^s) &= \text{Re} \int_{\Omega} \overline{u^s(\mathbf{x})}\delta u^s(\mathbf{x}) \\ & \quad \times \left[1 - \frac{|\alpha(\mathbf{x}_0)|}{|u^s(\mathbf{x})|} \right] \Delta_D(\mathbf{x} - \mathbf{x}_0) \, d\Omega(\mathbf{x}). \end{aligned} \tag{60}$$

It can be shown that $\Phi(\delta u^s)$ is a linear functional over the field of real numbers, and thus, the first variation of \mathcal{I} is [33]:

$$\delta\mathcal{I}(u^s; \delta u^s) = \Phi(u^s; \delta u^s). \tag{61}$$

Using (61), while restoring the definition (15) for the misfit functional \mathcal{J} , yields its first variation:

$$\begin{aligned} \delta_{u^s} \mathcal{J} &= \text{Re} \sum_{j=1}^{N_s} \int_{\Omega} \delta u^s(\mathbf{x}) \frac{\overline{u_m^s(\mathbf{x}_j)}}{|u_m^s(\mathbf{x}_j)|^2} \\ & \quad \times \left[1 - \frac{|u_m^s(\mathbf{x}_j)|}{|u^s(\mathbf{x})|} \right] \Delta_D(\mathbf{x} - \mathbf{x}_j) \, d\Omega(\mathbf{x}). \end{aligned} \tag{62}$$

Finally, we remark that station records are sampled only at locations for which $|u_m^s| \neq 0$, and thus the first denominator in (62) is well-behaved. Furthermore notice that the denominator $|u^s|$ in the third term of (62) corresponds to the computed response at the measurement stations, i.e., at $\mathbf{x} = \mathbf{x}_j$; in general, there may be shapes rendered by the inversion algorithm for which $|u^s(\mathbf{x}_j)|$ vanishes (silent zone). In such cases, the specific station could be removed from the inversion process; in practice, given the alignment of stations in the backscattered region, we have not encountered such difficulties.

8 Appendix II: on the proof of (37)

We rewrite the left-hand-side of (37) as:

$$\frac{\partial}{\partial \xi} \left(\frac{\partial u^{\text{inc}}}{\partial n} \right) = \nabla \dot{u}^{\text{inc}} \cdot \mathbf{n} + \nabla u^{\text{inc}} \cdot \dot{\mathbf{n}}. \tag{63}$$

Notice that $\dot{u}^{\text{inc}} = 0$, since the incident wave pressure is independent of Γ and its variations. Moreover (see, for example, [34]):

$$\left[\frac{D\mathbf{n}}{D\xi} \right]_{\xi=0} = \mathbf{n}^* = -\frac{\partial v_n}{\partial s} \mathbf{t} = \dot{\mathbf{n}} + v_n (\nabla \mathbf{n}) \mathbf{n}, \quad (64)$$

from which, there results:

$$\dot{\mathbf{n}} = -\frac{\partial v_n}{\partial s} \mathbf{t} - v_n (\nabla \mathbf{n}) \mathbf{n}. \quad (65)$$

Combining (63) and (65) yields:

$$\begin{aligned} \frac{\partial}{\partial \xi} \left(\frac{\partial u^{\text{inc}}}{\partial \mathbf{n}} \right) &= -\frac{\partial u^{\text{inc}}}{\partial s} \frac{\partial v_n}{\partial s} - \frac{\partial u^{\text{inc}}}{\partial s} v_n (\nabla \mathbf{n}) \mathbf{n} \cdot \mathbf{t} \\ &\quad - \frac{\partial u^{\text{inc}}}{\partial \mathbf{n}} v_n (\nabla \mathbf{n}) \mathbf{n} \cdot \mathbf{n}. \end{aligned} \quad (66)$$

Notice that it is easy to show that $(\nabla \mathbf{n})^T \mathbf{n} = 0$, and thus, by virtue of the identity $(\nabla \mathbf{n}) \mathbf{n} \cdot \mathbf{n} = \mathbf{n} \cdot (\nabla \mathbf{n})^T \mathbf{n}$, the last term in (66) vanishes. We use next the identity $(\nabla \mathbf{n} - (\nabla \mathbf{n})^T) \mathbf{n} = (\nabla \times \mathbf{n}) \times \mathbf{n}$ and multiply both sides of it by \mathbf{t} (inner product); there results:

$$\begin{aligned} (\nabla \mathbf{n}) \mathbf{n} \cdot \mathbf{t} &= [(\nabla \times \mathbf{n}) \times \mathbf{n}] \cdot \mathbf{t} = (\nabla \times \mathbf{n}) \cdot (\mathbf{n} \times \mathbf{t}) \\ &= \nabla \cdot [\mathbf{n} \times (\mathbf{n} \times \mathbf{t})] = \nabla \cdot [(\mathbf{n} \cdot \mathbf{t}) \mathbf{n} - (\mathbf{n} \cdot \mathbf{n}) \mathbf{t}] \\ &= -\nabla \cdot \mathbf{t} = -\text{div} \mathbf{t}, \end{aligned} \quad (67)$$

where various vector identities have been used. Substituting (67) in (66) yields (37).

References

- Bonnet M (1995) BIE and material differentiation applied to the formulation of obstacle inverse problem. *Eng Anal Bound Elem* 15:121–136
- Guzina B, Fata SN, Bonnet M (2002) An elastodynamic boundary element approach for underground cavity identification. In: *Proceedings of IABEM 2002*, Austin, TX
- Guzina B, Fata SN, Bonnet M (2003) On the stress-wave imaging of cavities in a semi-infinite solid. *Int J Solids Struct* 40:1505–1523
- Fata SN, Guzina B, Bonnet M (2003) Computational framework for the BIE solution to inverse scattering problems in elastodynamics. *Comput Mech* 32:370–380
- Colton D, Kress R (1983) *Integral equation methods in scattering theory*. Wiley-Interscience, New York
- Colton D, Kress R (1998) *Inverse acoustic and electromagnetic scattering theory*, 2nd edn. Springer, New York
- Kirsch A (1996) *An introduction to the mathematical theory of inverse problems*. Springer, Heidelberg
- Pike R, Sabatier P (2002) (eds) *Scattering: scattering and inverse scattering in pure and applied science*, vols 1 and 2. Academic, San Diego
- Colton D, Coyle J, Monk P (2000) Recent developments in inverse scattering theory. *SIAM Rev* 42:369–414
- Maponi P, Recchioni M, Zirilli F (1997) The use of optimization in the reconstruction of obstacles from acoustic or electromagnetic scattering data. In: Biegler L (ed) et al *Large scale optimization with applications*, IMA Vol. Math. Appl.. Springer, New York, pp 81–100
- Angell TS, Jiang X, Kleinman RE (1997) A distributed source method for inverse acoustic scattering. *Inverse Probl* 13:531–545
- Hass M, Rieger W, Lehner G (1997) Inverse 3D acoustic and electromagnetic obstacle scattering by iterative adaption. In: Chavent G, Sabatier P (eds) *Inverse problems in wave propagation and diffraction*. Springer, Berlin, pp 204–215
- Kress R, Zinn A (1992) On the numerical solution of the three dimensional inverse obstacle scattering problem. *J Comput Appl Math* 42:49–61
- Maponi P, Misici L, Zirilli F (1991) An inverse problem for the three dimensional vector Helmholtz equation for a perfectly conduction obstacle. *J Comput Math Appl* 22:137–146
- Misici L, Zirilli F (1994) Three dimensional inverse obstacle scattering for time harmonic acoustic waves: A numerical method. *SIAM J Sci Comput* 15:1174–1189
- Zinn A (1989) On an optimisation method for the full- and the limited-aperture problem in inverse acoustic scattering for a sound-soft obstacle. *Inverse Probl* 5:239–253
- Kress R, Rundell W (1994) A quasi-Newton method in inverse obstacle scattering. *Inverse Probl* 10:1145–1157
- Kress R (1995) Integral equation methods in inverse obstacle scattering. *Eng Anal Bound Elem* 15:171–179
- Colton D, Kirsch A (1996) A simple method for solving inverse scattering problems in the resonance region. *Inverse Probl* 12:383–393
- Colton D, Piana M, Potthast R (1997) A simple method using Morozov's discrepancy principle for solving inverse scattering problems. *Inverse Probl* 13:1477–1493
- Colton D, Giebermann K, Monk P (2000) A regularized sampling method for solving three-dimensional inverse scattering problems. *SIAM J Sci Comput* 21:2316–2330
- Potthast R (1998) A point-source method for inverse acoustic and electromagnetic obstacle scattering problems. *IMA J Appl Math* 61:119–140
- Potthast R (1996) A fast new method to solve inverse scattering problems. *Inverse Probl* 12:731–742
- Burton AJ, Miller GF (1971) The application of integral equation methods to the numerical solution of some exterior boundary-value problems. *Proc R Soc Lond* 323:201–210
- Brakhage H, Werner P (1965) Über das Dirichlet- sche Aussenraumproblem für die Helmholtzsche Schwingungsgleichung. *Arch Math* 16:325–329
- Bielak J, MacCamy RC, Zeng X (1995) Stable coupling method for interface scattering problems by combined integral equations and finite elements. *J Comput Phys* 119:374–384
- Kallivokas LF, Na S-W (2005) Continuation schemes for shape detection in inverse acoustic scattering problems. *Eng Anal Bound Elem* (accepted)
- Karush W (1939) *Minima of functions of several variables with inequalities as side constraints*. Master Thesis, University of Chicago, Chicago, IL
- Kuhn HW, Tucker AW (1951) *Nonlinear programming*. In: Neyman J (ed) *Proceedings of the 2nd Berkeley symposium on mathematical statistics and probability*. University of California Press
- Petryk H, Mróz Z (1986) Time derivatives of integrals and functionals defined on varying volume and surface domains. *Arch Mech* 38:697–724
- Kirsch A, Kress R, Monk P, Zinn A (1988) Two methods for solving the inverse acoustic scattering problem. *Inverse Probl* 4:749–770
- Colton D, Kirsch A (1996) A simple method for solving inverse scattering problems in the resonance region. *Inverse Probl* 12:383–393
- Gelfand IM, Fomin SV (translated by Silverman RA) (2000) *Calculus of variations*. Dover Publications, New York
- Kosinski W (translated by Ogden RW) (1986) *Field singularities and wave analysis in continuum mechanics*. Wiley and Polish Scientific Publishers, New York